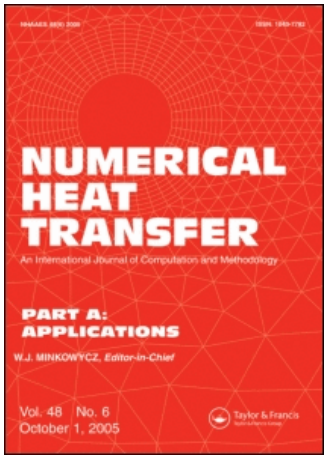

Numerical Heat Transfer, Part A: Applications
An International Journal of Computation and Methodology
Publication details, including instructions for authors and subscription information:
http://www.informaworld.com/smpp/title~content=t713657973

Numerical Studies on Combustion Characteristics of Interacting Pulverized Coal Particles at Various Oxygen Concentration

Chong Pyo Cho [a]; Sangpil Jo [a]; Ho Young Kim [a]; Sam S. Yoon [a]
[a] Department of Mechanical Engineering, Korea University, Seoul, Korea

Online Publication Date: 01 January 2007
To cite this Article: Cho, Chong Pyo, Jo, Sangpil, Kim, Ho Young and Yoon, Sam S. (2007) 'Numerical Studies on Combustion Characteristics of Interacting Pulverized Coal Particles at Various Oxygen Concentration', Numerical Heat Transfer, Part A: Applications, 52:12, 1101 - 1122
To link to this article: DOI: 10.1080/10407780701446549
URL: http://dx.doi.org/10.1080/10407780701446549

Numerical Heat Transfer, Part A, 52: 1101–1122, 2007

ISSN: 1040-7782 print/1521-0634 online
DOI: 10.1080/10407780701446549

Taylor & Francis
Taylor & Francis Group

NUMERICAL STUDIES ON COMBUSTION CHARACTERISTICS OF INTERACTING PULVERIZED COAL PARTICLES AT VARIOUS OXYGEN CONCENTRATION

Chong Pyo Cho, Sangpil Jo, Ho Young Kim, and Sam S. Yoon
Department of Mechanical Engineering, Korea University, Seoul, Korea

The two-dimensional laminar combustion characteristics of coal particles at various oxygen concentration levels of a surrounding gas have been numerically investigated. The numerical simulations, which use the two-step global reaction model to account for the surrounding gas effect, show the detailed interaction among the inter-spaced particles, undergoing devolatilization and subsequent char burning. Several parametric studies, which include the effects of gas temperature (1700 K), oxygen concentration, and variation in geometrical arrangement of the particles on the volatile release rate and the char burning rate, have been carried out. To address the change in the geometrical arrangement effect, multiple particles are located at various inter-spacings of 4–20 particle radii in both streamwise and spanwise directions. The results for the case of multiple particles are compared with those for the case of a single particle. The comparison indicates that the shift to the multiple particle arrangement resulted in the substantial change of the combustion characteristics and that the volatile release rate of the interacting coal particles exhibits a strong dependency on the particle spacing. The char combustion rate is controlled by the level of oxygen concentration and gas composition near particles during combustion. The char combustion rate is highly dependent on the particle spacing at all oxygen levels. The correlations of the volatile release rate and the change in total mass of particles are also found.

1. INTRODUCTION

Blast furnaces using pulverized coals have widely been used in various industrial applications due to their high thermal efficiency. Pulverized coals are injected into a blowpipe through the pre-heated hot air stream [1]. The mixing process of the pulverized coals and the hot air stream influences the behavior of the coal diffusion flame. Most analyses of pulverized coal combustion in a furnace have focused on the single particle combustion even though, in reality, multi-particle combustion is significantly different from the single particle combustion. The difference between group combustion characteristics and single particle combustion characteristics is due to the fact that the interaction among coal particles and the particle-gas interaction affect the net devolatilization rate and their subsequent char burning. Single coal particle combustion [2–5] has been experimented and modeled extensively,

Received 22 October 2006; accepted 9 March 2007.
Address correspondence to Ho Young Kim, Department of Mechanical Engineering, 5-ga, Anam dong, Sungbuk-gu, Seoul 136-701, Korea. E-mail: kimhy@korea.ac.kr

NOMENCLATURE

A	surface area of spherical particle
C_p	specific heat
D	particle (or cylinder) diameter, $2R_0$ or binary diffusivity
k	thermal conductivity
m_p	coal particle mass
R_0	initial particle radius
w_k	mass production or consumption rate of species k
X	horizontal particle spacing, nondimensionalized by particle radius
x	dimensionless streamwise coordinate
Y	vertical particle spacing, nondimensionalized by particle radius
Y_k	Mass fraction of a species
y	dimensionless spanwise coordinates
χ	mole fraction
ν	dynamic viscosity, μ/ρ
ρ	density

Subscripts

c	fixed carbon
d	dry and ash free coal or particle diameter
k	chemical species
p	particle
v	volatile fuel
m	multiple particle property
s	single particle property

Superscripts

*	dimensionless value

but the results of these efforts have not contributed to the understanding of multi-particle combustion, especially in highly convective environment. The objective of the current study is to numerically describe the burning behavior of the multi-particle combustion at varying devolatilization rates and the subsequent char burning for the given group combustion environment. The computational results, obtained from the single combustion and the multi-particle combustion simulation, are correlated as a function of geometrical variance (i.e., inter-particle spacing) and O_2 concentration level.

2. MATHEMATICAL MODEL DESCRIPTION

2.1. Governing Equations for Gas Phase

Figure 1 shows the physical configuration of the calculation conducted herein. As shown, the coal particles, exposed to a freely convective flow of high temperature,

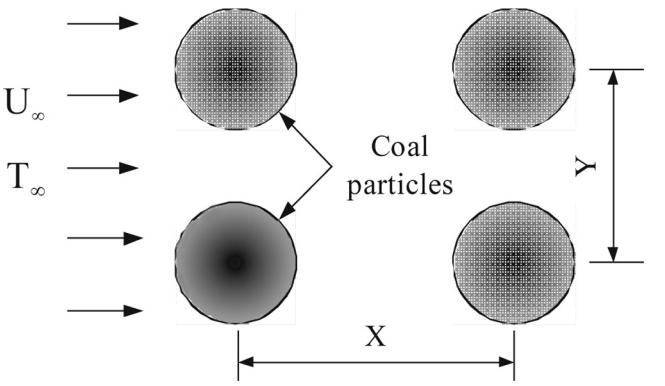

Figure 1. Schematic of coal particles burning in a convective flow.

going from left to right, are evenly spaced in both x and y directions. It is assumed that the buoyancy effect due to gravity is smaller than that of the free stream convection. Because this study aims to examine the effect of multi-particle interaction, a 2-D Cartesian coordinate is more suitable than the axi-symmetric coordinate system, which would have been more desirable for a single particle interaction simulation. The 2-D governing equations, listing conservation of mass, momentum, energy, and species, for the gas phase are given as follows.

$$\frac{\partial \rho}{\partial t} + \frac{\partial}{\partial x_j}\left\{\rho\left(u_j - \frac{\partial x_j}{\partial t}\right)\right\} = 0 \tag{1}$$

$$\frac{\partial \rho}{\partial t} + \frac{\partial}{\partial x_j}\left\{\rho\left(u_j - \frac{\partial x_j}{\partial t}\right)u_i\right\} = \frac{\partial}{\partial x_j}\left[\mu\left(\frac{\partial u_j}{\partial x_i} + \frac{\partial u_i}{\partial x_j}\right)\right] - \frac{\partial p}{\partial x_i} \tag{2}$$

$$\frac{\partial}{\partial t}(\rho h) + \frac{\partial}{\partial x_j}\left\{\rho\left(u_j - \frac{\partial x_j}{\partial t}\right)h\right\} = \frac{\partial}{\partial x_j}\left(\frac{k}{c_p}\frac{\partial h}{\partial x_j}\right) + \sum h_{0k}\nu_k w_k \tag{3}$$

$$\frac{\partial}{\partial t}(\rho Y_k) + \frac{\partial}{\partial x_j}\left\{\rho\left(u_j - \frac{\partial x_j}{\partial t}\right)Y_k\right\} = \frac{\partial}{\partial x_j}\left(\rho D\frac{\partial Y_k}{\partial x_j}\right) - \nu_k w_k \tag{4}$$

The governing equations using the orthogonal coordinates have been transformed into general curvilinear coordinates. The equation of state of Peng-Robinson [6] is used herein. The governing equations of gas phase are discretized into their algebraic counterparts based on the finite-volume method. Then, the SIMPLEC algorithm is used to solve gas flow, where the power-law scheme is used for the convective and diffusive flux terms. The (strongly implicit procedure) SIP method [7] is used to guarantee numerical stability. To simulate the volatilization of methane, CH_4, the two-step global finite-rate chemical reaction model is also utilized [8]. The stoichiometric reaction equations for the oxidation of methane and carbon monoxide (CO) are written as follows.

$$CH_4 + 1.5O_2 \rightarrow CO + 2H_2O \tag{5}$$

$$CO + 0.5O_2 \rightarrow CO_2 \tag{6}$$

More detailed descriptions on the reaction rate of the gas phase are available in refs. [8, 9].

2.2. Governing Equations for Solid Phase

The temperature of all particles is initially set constant, but it varies as time increases. The mass and energy equations for the particle phase are given as follows.

$$\frac{\partial m_p}{\partial t} = -\int \sum \dot{m}_c'' dA - \dot{m}_v \tag{7}$$

$$m_p C_{p,c} \frac{\partial T_p}{\partial t} = \int \Delta h_c \dot{m}_c'' dA + \Delta h_v \dot{m}_v + \int k \frac{\partial T}{\partial n} dA \tag{8}$$

where $\dot{m}_c''$ and $\dot{m}_v$ represent the char oxidation rate and devolatilization rate, respectively. No soot is present in the volatilizing region because of the ideal complete combustion in the gas phase. The radiation effect is less dominant when the particle size increases for the particle size approaching 100 μm [4]. To simplify our analysis and to focus on the influence of geometrical variation on combustion characteristics, radiation effect is not considered in the current study. The specific heat of ash-free coal, $C_{p,c}(T_p)$, is calculated by using the Merrick's method [10].

2.3. Devolatilization Rate

The coal devolatilization rate is calculated by using the two-competing-reactions model of ref. [11]. The volatile release rate is expressed as follows.

$$\dot{m}_v = -m_d(\alpha_1 R_1 + \alpha_2 R_2) \tag{9}$$

$$\dot{m}_d = -m_d(R_1 + R_2) \tag{10}$$

$$R_i = A_i \exp(-E_i/RT_p), \quad i = 1, 2 \tag{11}$$

Here, α_1 and α_2 are known as adjustable constants, that provides larger degree of freedom for a model user [11]. α_1 represents the fraction of the volatile; the value of $\alpha_1 = 0.38$, which is currently used for all runs, according to the proximate analysis [11]. Table 1 indicates the weight-portions of volatile, fixed-carbon, moisture, and ash of a typical coal particle. The current model employs the dry-ash-free, so called, *daf* model, [3] which yields approximately 40% and 60% weight-portions for volatile and fixed-carbon, respectively. As for α_2, 0.8 is normally used to induce rapid reaction.

2.4. Heterogeneous Carbon Reactions

The following three types of heterogeneous char reaction at particle surface are used [12, 13].

$$\mathrm{C} + \mathrm{O_2} \rightarrow \mathrm{CO_2} + 1.287 \times 10^7 \ (\mathrm{J/kg}) \tag{12}$$

$$2\mathrm{C} + \mathrm{O_2} \rightarrow 2\mathrm{CO} + 1.865 \times 10^7 \ (\mathrm{J/kg}) \tag{13}$$

$$\mathrm{C} + \mathrm{CO_2} \rightarrow 2\mathrm{CO} - 1.415 \times 10^7 \ (\mathrm{J/kg}) \tag{14}$$

Table 1. Proximate analysis of coal (wt.%)

Volatile	Fixed carbon	Moisture	Ash
35.4	51.7	8.4	4.5

Table 2. Kinetics constants [12, 13]

	$R = A\exp(-E/RT)$		
Reaction	A	Unit	E (J/kmol)
Devolatilization rate 1	3.7×10^5	s^{-1}	7.366×10^7
Devolatilization rate 2	1.46×10^{13}	s^{-1}	2.511×10^8
Char reaction 1	1.225×10^3	$m\ s^{-1}$	9.977×10^7
Char reaction 2	3.007×10^5	$m\ s^{-1}$	2.477×10^8
Char reaction 3	4.016×10^8	$m\ s^{-1}$	1.255×10^8

The char reaction rates for the above reactions are given as follows.

$$\dot{m}''_{c1} = -(1/\beta_{c1})\rho_s Y_{O_2,s} A_{c1} \exp(-E_{c1}/RT_p) \tag{15}$$

$$\dot{m}''_{c2} = -(1/\beta_{c2})\rho_s Y_{O_2,s} A_{c2} \exp(-E_{c2}/RT_p) \tag{16}$$

$$\dot{m}''_{c3} = -(1/\beta_{c3})\rho_s Y_{CO_2,s} A_{c3} \exp(-E_{c3}/RT_p) \tag{17}$$

Thus, the total species reaction rates on the particle surface are written as below.

$$\dot{m}_c = \int (\dot{m}''_{c1} + \dot{m}''_{c2} + \dot{m}''_{c3})\, dA \tag{18}$$

$$\dot{m}''_{O_2} = \beta_{c1}\dot{m}''_{c1} + \beta_{c2}\dot{m}''_{c2} \tag{19}$$

$$\dot{m}''_{CO_2} = -(1 + \beta_{c1})\dot{m}''_{c1} + \beta_{c3}\dot{m}''_{c3} \tag{20}$$

$$\dot{m}''_{CO} = -(1 + \beta_{c2})\dot{m}''_{c2} - (1 + \beta_{c3})\dot{m}''_{c3} \tag{21}$$

where β_{c1}, β_{c2} and β_{c3} represent the stoichiometric ratios for the char reactions on the particle surface. The kinetic constants of these reactions are given in Table 2.

2.5. Initial and Boundary Conditions

All coal particles are assumed to be spherical in shape and its temperature is initially set as 600 K, considering the pre-heated process. The particle size is set to decrease spherically when the particle loses its mass during combustion [14]. Blowing-velocity of volatile fuel from the particle surface is calculated by using the volatile release rate, char burning rate, and shrinkage rate of a coal particle. The initial oxygen mass fraction at the particle surface is set to be same as that of the free stream condition. The mass fraction of other species can be recalculated when the homogeneous and heterogeneous reactions occur:

$$Y_{CO_2,s} = Y_{CO_2,g} + m_{CO_2,s}/m_g \tag{22}$$

$$Y_{CO,s} = Y_{CO,g} + m_{CO,s}/m_g \tag{23}$$

$$Y_{O_2,s} = Y_{O_2,g} + m_{O_2,s}/m_g \tag{24}$$

where $m_{CO_2,s}$, $m_{CO,s}$ and $m_{O_2,s}$ represent the mass loss or formation by the heterogeneous reactions at the surface for CO_2, CO, and O_2, respectively. m_g is the total gas mass on the particle surface.

3. RESULTS AND DISCUSSIONS

The coal particles were fixed in space in a freely convective gas flow of high temperature and in 1 atmospheric pressure environment. The mole concentration of O_2 ranged from 15% to 95%. The range of the Reynolds number, based on the particle diameter, was $1 < \mathrm{Re} < 5$, which was consistent with the operating range of the previous experimental data of ref. [2]. The geometrical variance, defined with X and Y as in Figure 1, ranged from 2 to 10 particle diameter. The Illinois No. 6 coal, which was studied in ref. [2], was used in the current simulations. The symmetric boundary conditions are applied to the upper and lower limits of the computational domain to replicate the presence of neighbor particles above and below, as shown in Figure 2. All simulations ran for a duration of around 40 ms ($\pm$10 ms) on $28R_0 < x < 46R_0$ and $2R_0 < y < 12R_0$ domains in the x and y directions, respectively. A Cartesian grid of 370×60 was employed, the resolution of which seemed to be acceptable based on the grid sensitivity, as shown in Figure 3. The smallest grid size used was $\Delta x_{\min} = 0.01R_0$ with the time step of $\Delta t = 5.56\,\mu s$.

Prior to simulating the particle combustion, the two-dimensional code is first verified by applying the flow over cylinder case, which has been popularly studied by numerous researchers. We verified the current code by comparing our computational results against the work of refs. [15–17]. The operating Reynolds number is $\mathrm{Re}_{cyl} = UD/v = 40$, where D is the cylinder diameter (or $2R_0$). Here, the geometrical parameters (i.e., the wave size, inter-distance and location of the vortices, and flow separation point, as in Figure 4) of the wake or recirculated region are computed. Note that Figure 4 is the actual computed result, not a schematic. The comparisons

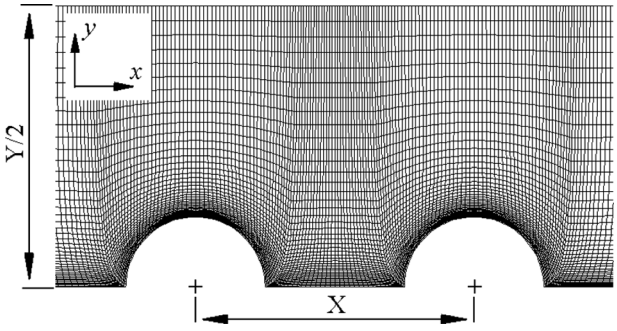

Figure 2. Grid system of coal particles.

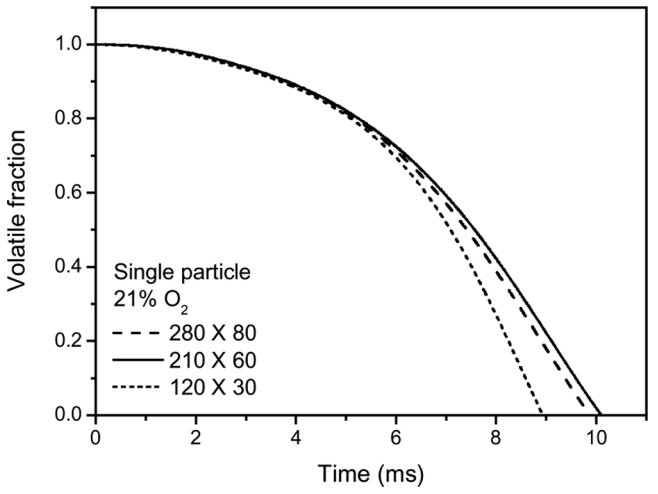

Figure 3. Variation of volatile fraction obtained by various numerical grids.

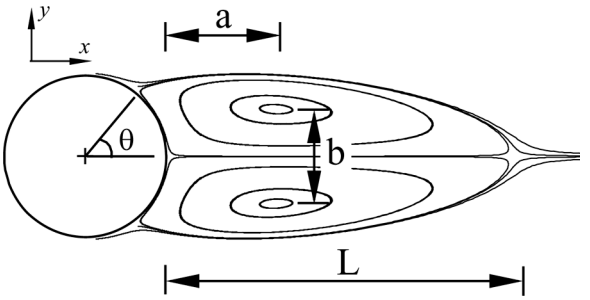

Figure 4. Streamlines for $Re_{cyl} = 40$ and definition of wake parameters.

indicate that the current code is capable of predicting the results within 0.1–4.2% error, based on the standard deviation, as in Table 3. The model is verified for the case of flow over cylinder condition, and the model validation using the experimental data for the particle combustion case will be presented in Section 3.1.

Table 3. Comparison present results with those of other published papers for Re = 40

	Constanceau and Bouard [15]	Rengel and Sphaier [16]	Wanderley and Levi [17]	Present study	Standard deviation
C_d	N.A.	1.61	1.60	1.65	0.022
L/D	2.13	2.23	2.10	2.16	0.048
a/D	0.76	0.72	0.69	0.69	0.029
b/D	0.59	0.58	0.58	0.59	0.005
θ	53.50	54.06	53.20	53.55	0.309

3.1. Effect of Oxygen Concentration

When the particle temperature increases due to heat transfer from the hot gas (or bulk flow), volatiles released from the particle are formed around the particle surface in the region called Region 1, as in Figure 5. Regions 1 and 2 constitute the devolatilization stage, while Region 3 indicates the char combustion process. One noticeable behavior is that the char combustion occurs at a faster rate when the O_2 concentration is increased; the time at which the combustion occurs for 95% and 15% O_2 concentration is approximately 4 ms and 12 ms, respectively.

Because of these volatiles of relatively cooler temperature and the endothermic heat of reaction for each of the two devolatilization reactions, the increasing temperature gradient of the particle is slightly reduced in the region called Region 2, as indicated in Figure 5, for the single particle case. Heat obtained from the burning of volatiles is fed back onto the particle surface and, therefore, the particle temperature and devolatilization rate are further increased. As the devolatilization rate increases, the mass fraction of O_2 on the particle surface sharply decreases due to its mass loss in burning, noted with the devolatilization range of the upper 40% mass loss in Figure 6*a*. O_2 is further depleted because the volatile ejection pushes the O_2 away from the particle. Also, O_2 may be depleted because the supplied oxygen from the bulk flow is mostly consumed in a flame surrounding the particle. Note that, for a given O_2 concentration, a rapid change in the particle mass fraction of Figure 6*a* is consistent with that in the particle temperature of Figure 5 at their shift range of 4–12 ms. Also note that the greater the O_2 concentration, the shorter the devolatilization period and, thus, earlier and faster the char combustion.

During the devolatilization process, the char combustion, whose heterogeneous reaction requires O_2 supply as indicated in Eqs. (12) and (13), on the particle surface is restrained because of O_2 depletion in the region. At the end of the devolatilization process, the particle temperature rapidly increases to the flame temperature, close to

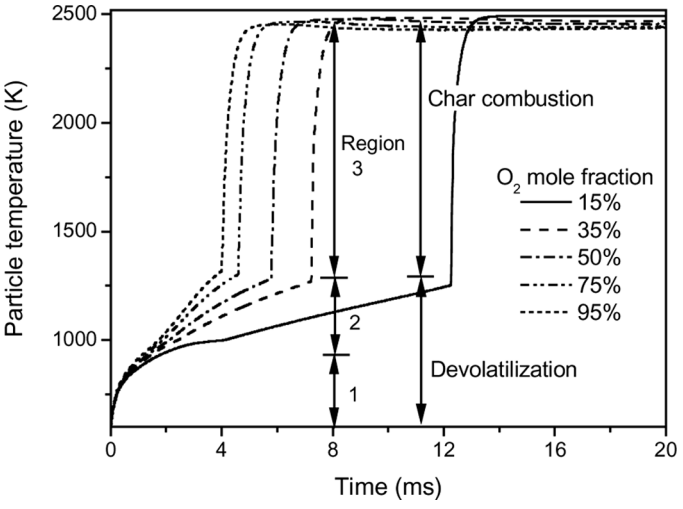

Figure 5. Temperature histories of single coal particle for various O_2 concentrations.

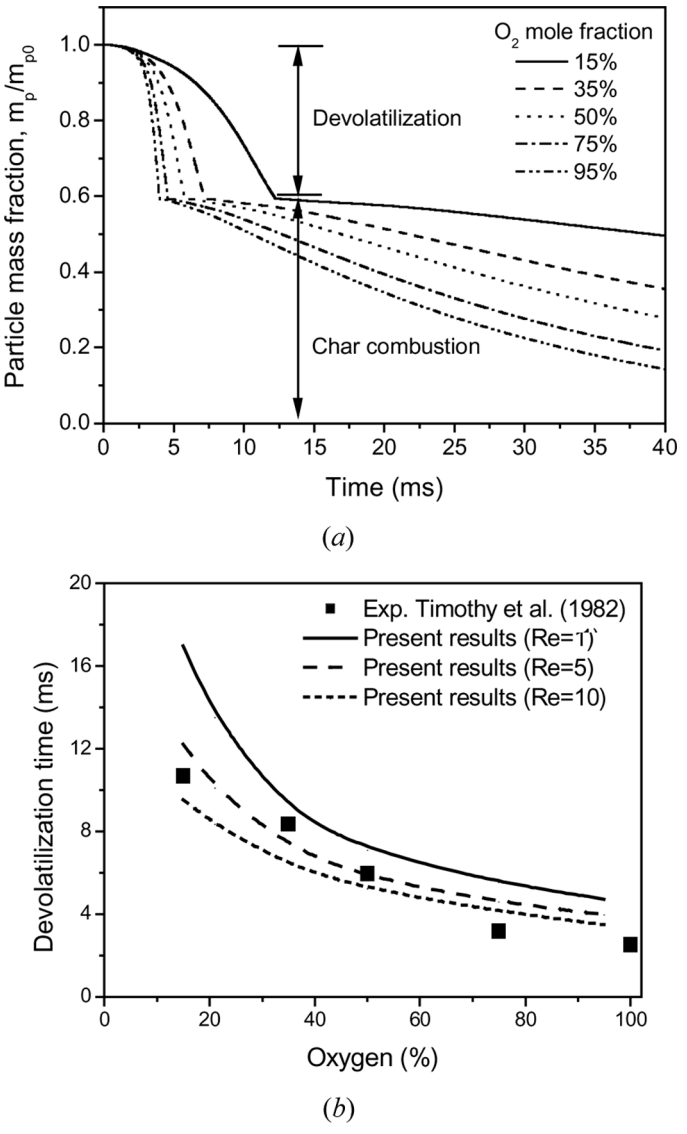

Figure 6. *a*) Particle mass fraction histories for various O_2 concentration and *b*) devolatilization time versus O_2 concentration for various Reynolds number.

~ 2500 K, as in Figure 5 (see the peak in Region 3). Predictions by the current model are validated with the experimental data: Figure 6*b* shows the devolatilization time (or period) for a single coal particle combustion at various oxygen concentrations, the results of which are in good agreement with previously obtained experimental data obtained for a relatively low Reynolds number, ranging $1 < \mathrm{Re} \leq 10$.

At higher O_2 concentration (i.e., 35%), the envelope-flame, depicted with white color in Figure 7*a*, is in closer touch with the particle surface than the flame with

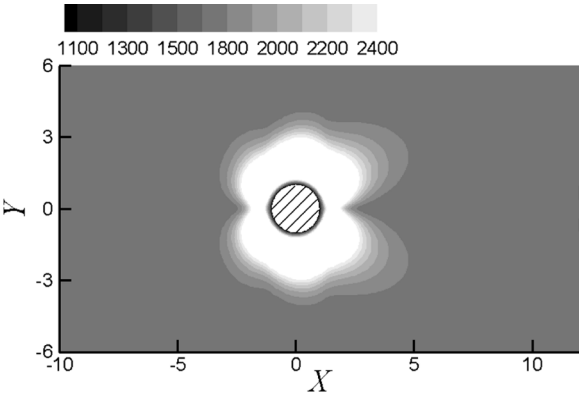

(*a*) 35% O_2

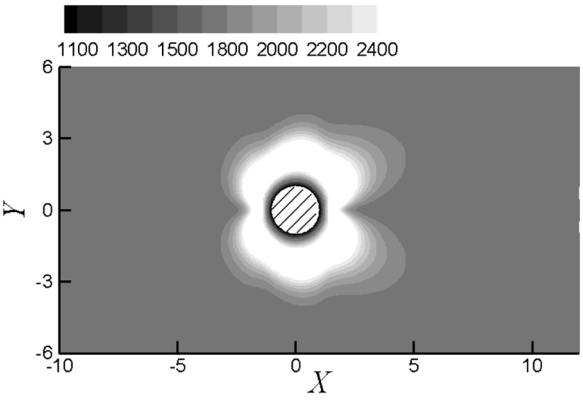

(*b*) 15% O_2

Figure 7. Temperature contours with O_2 concentration in air at 1.8 ms: (*a*) 35% O_2, and (*b*) 15% O_2.

smaller O_2 concentration (see Figure 7*b*). During the char combustion process, the enlarged CO layer, produced from the char reaction of Eq. (13), is reacted with the incoming O_2 as indicated in Eq. (6). As a result, O_2 is mostly consumed at the outer surface of the CO layer. Meanwhile, CO is also consumed during the reaction process of Eq. (6). At this point, O_2 penetration to the particle surface becomes easier due to the partial removal of the CO layer. Then, O_2 is reacted with the carbon as in Eq. (13) and their reaction produces the CO layer again around the particle's immediate surface and, thus, the CO layer is enlarged again. This recurrent process continues during char combustion process until the complete combustion of the particle, as indicated by the continual frequent peaks of the surface mass flux histories in Figure 8. As shown, when O_2 concentration is increased, the burning of the volatiles is greatly enhanced as the particle surface mass flux is greater for all time. Note that the similar trends corresponding to O_2 concentration of 75% and 95% are not shown in Figure 8 for clarity.

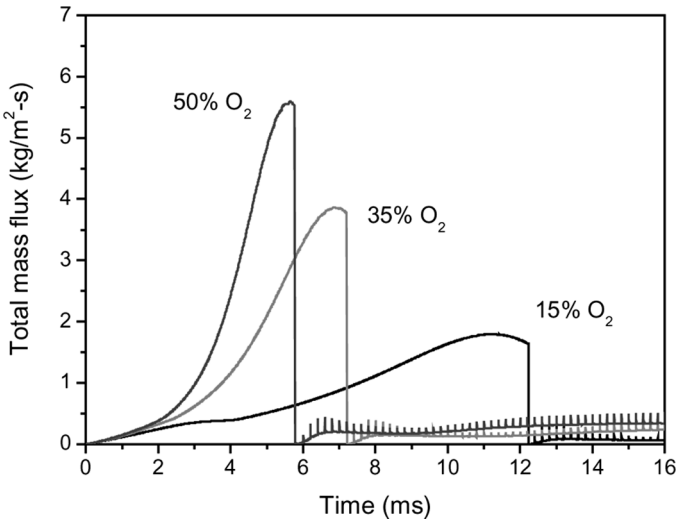

Figure 8. Total mass and flux on the particle surface for various O_2 concentrations.

3.2. Effects of Inter-Particle Spacing on Volatile Release Rate

Figure 9 shows the snapshot of the flame configuration at 4 ms in the devolatilization process. The O_2 concentration of the surrounding gas is at 15% and the horizontal spacing, X, between particles is set as 4 and as 10 for Figures 9*a* and 9*b*, respectively. Here the first and second particles are referred to as the ones located upstream and downstream, respectively. At the early stage of the combustion process, envelope-flames are formed around the particles. As the envelope-flames branch out, the flames are conglomerated into one single flame. When X is reduced, the single flame appears comparably faster than the case with larger X, indicative of group combustion characteristics when particles are closely situated.

The temperature increase of particles inside the single flame, especially the second particle, is slowed down because of the volatiles of relatively low temperature. The reduced convection effect (i.e., insufficient O_2 delivery) due to the second particle location is another reason for the lower temperature of the second particle. Figure 10 shows the nature of the second particle's lower temperature, as compared with that of the first or single particle at 15% O_2 concentration; here, the first particle combustion characteristics are nearly the same as those of the single particle and, thus, their lines overlap. When these two particles are located farther with increasing X, then the trend of the second particle combustion characteristic is leaning toward that of the single particle. However, when $X = 20$, the trend is, in fact, reversed, which is unexpected. This sudden change in the trend is related with the endothermic process of Eq. (14) during the heterogeneous reaction. Further details on this issue will be explored and explained in Section 3.3.

Figure 11 shows the snapshot of the flame configuration at 9 ms, in the devolatilization process; the char combustion is not initiated up until 12 ms at 15% O_2 concentration as indicated in Figure 6*a*. The surrounding O_2 concentration is at 15% and the vertical spacing, Y, between particles was set as 4 and 6 for

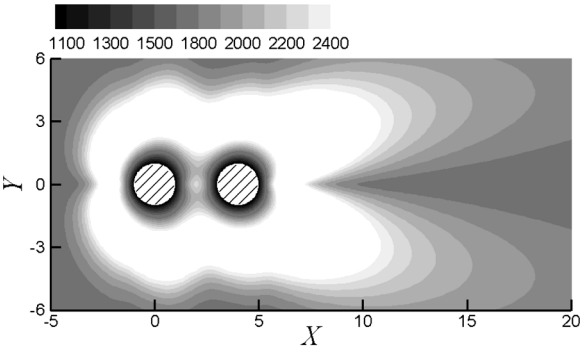

(*a*) X = 4

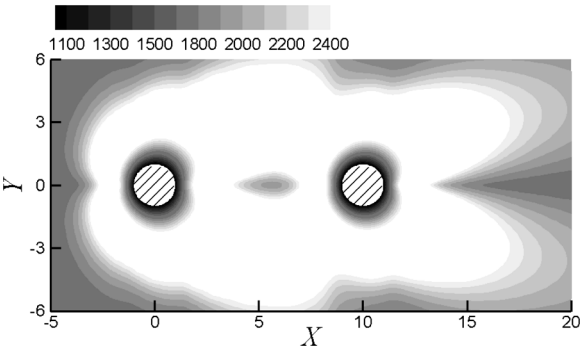

(*b*) X = 10

Figure 9. Temperature contours with horizontal particle spacing at 15% O_2 air ($Y = 20$, 4 ms).

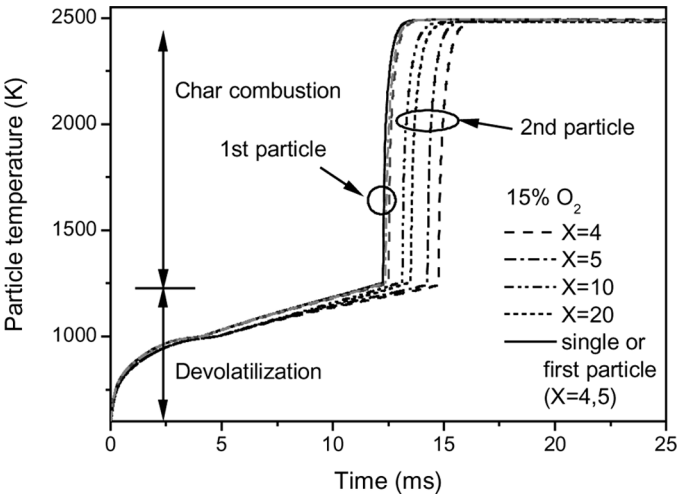

Figure 10. Temperature histories of the second particle with horizontal particle spacing at 15% O_2 air.

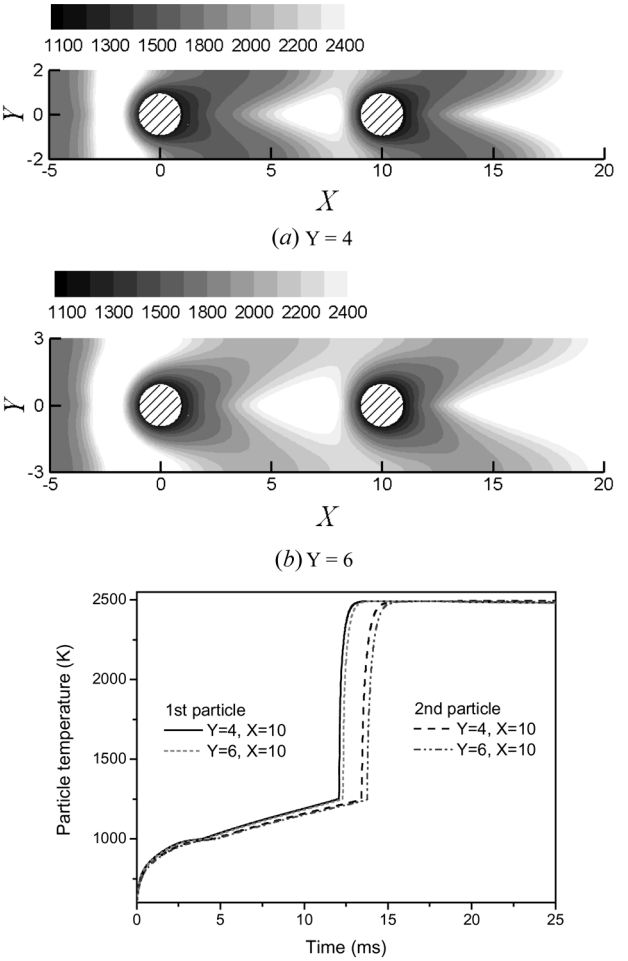

Figure 11. Temperature contours with vertical particle spacing at 15% O_2 air ($X = 10$, 9 ms): *a*) $Y = 4$, *b*) $Y = 6$, *c*) comparison of the first and second particle temperature histories when Y is reduced.

Figures 11*a* and 11*b*, respectively, with fixed $X = 10$. Symmetric boundary conditions are applied to the upper and lower limits of the computational domain to replicate the presence of neighbor particles above and below. When the O_2 concentration is 15%, it is observed that the individual particle flames are merged with those of their neighbor particles at smaller Y; this mergence is shown in Figures 11*a* and 11*b*. The region between two particles is overshadowed (relatively larger "darker" area) and closely connected by the larger amount of volatiles of relatively lower temperature in Figure 11*a*, whose characteristics eventually lead to group combustion in a later time. Meanwhile, this so called in-between region becomes less overshadowed by the volatile when Y is increased and, thus, the region of high temperature between particles is more predominant (larger white area).

In Figure 11*a*, volatiles are released from the first particle are convected downstream, toward the second particle. During this drift, O_2 between particles is consumed and, consequently, the flame between particles becomes extinguished. Because of the accelerated convection through the squeezed channel in the case of the reduced Y value, the first particle is subject to enhanced heat transfer and, thus, its temperature and devolatilization rate are increased; see Figure 11*c* for higher temperatures of the first and second particles. The first particle temperature is generally larger than that of the second because of the following reasons. First, the sufficient O_2 supply near front of the first particle enhances the combustion, and this enhancement induces more volatile emission of the low temperature. Second, these released volatiles are drifted downstream and reduce the temperature near the second particle. Further, because of the volume occupation of these volatiles, sufficient O_2 supply near the second particle region is prevented.

The volatile release rates, $\dot{V}_{1,2} = dV_{1,2}/dt\big|_{15\%}$, of the first and second particles at 15% O_2 concentration are plotted on X-Y parametric dimensions (which differ from *x*-*y* coordinate dimensions) as in Figures 12*a* and 12*b*, respectively. The volatile

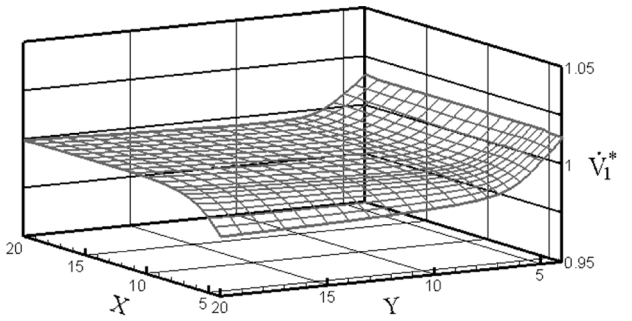

(*a*) 1st particle

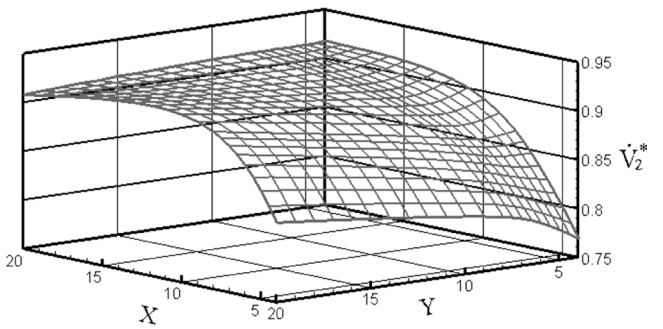

(*b*) 2nd particle

Figure 12. Relative volatile release rate of interacting particle to that of single particle at 15% O_2 air: *a*) first particle and *b*) second particle.

release rate of the multiple particles is non-dimensionalized by the single particle volatile release rate of the corresponding O_2 concentration, $\dot{V}_s = dV_s/dt|_{15\%}$. When X is reduced as in Figure 12*a*, $\dot{V}_1^*$ is also reduced due to the accumulation of the volatiles of low temperature for most of the Y range. However, when Y is smaller than 6, $\dot{V}_1^*$ increases and reaches up to around $\dot{V}_1^* = 1.015$ at $Y = 4$, because the flow acceleration due to the smaller Y causes greater heat transfer (i.e., convection) through the squeezed channel. At this small Y, the enhanced heat transfer effect is the greater driving mechanism over the competing effect of the volatile accumulation, which occurs at small X. This cross-change occurs at around $Y = 6$, as mentioned above.

Figure 12*b* also shows $\dot{V}_2^*$ behavior at various X and Y. When X is reduced, $\dot{V}_2^*$ is also decreased. Further, when Y is reduced at a smaller X, $\dot{V}_2^*$ reduces more, reaching its value down to approximately $\dot{V}_2^* = 0.77$. The reason for this behavior is previously explained in detail in discussion of Figure 11; as the Y decreases, the second particle receives more volatiles from the first.

One may further scrutinize the $\dot{V}_{1,2}^*$ behavior on the X-Y map while observing the results obtained at different O_2 concentrations. Figure 13 shows the $\dot{V}_{1,2}^*$ pattern

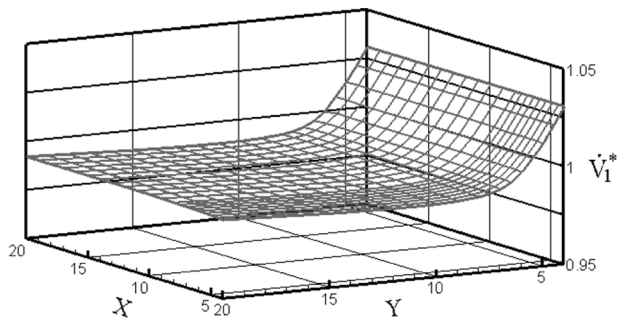

(*a*) 1st particle

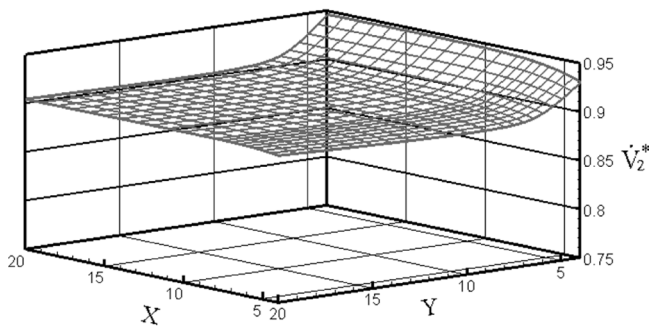

(*b*) 2nd particle

Figure 13. Relative volatile release rate of interacting particle to that of single particle at 50% O_2 air: *a*) first particle and *b*) second particle.

at increased O_2 concentration, 50%. While comparing $\dot{V}_1^*$ of the first particle at 15% and 50% O_2 concentrations, in Figure 12*a* and Figure 13*a*, respectively, one may see that $\dot{V}_1^*$ is little affected by the reduction of X at 50% O_2, a result that is different from that of the case with 15% O_2. It seems that the variation in X cannot influence the $\dot{V}_1^*$ of the first particle at higher O_2 concentration. The reason may be as follow: first, at higher O_2 concentration, the hot flame zone (the white zone as in Figure 7) approaches to the particle surface closer and, thus, the volatile accumulation due to the reduction of X is prevented. Second, volatile consumption is further increased with a larger flame at higher O_2. The effect caused by flow acceleration at reduction of Y is also manifest in Figure 13*a*. This increase in $\dot{V}_1^*$ is only magnified when O_2 concentration is increased, shifting its value from $\dot{V}_1^* = 1.015$ of Figure 12*a* to $\dot{V}_1^* = 1.03$ of Figure 13*a* for $Y = 4$.

Figure 13*b* indicates that $\dot{V}_2^*$ of the second particle is independent of X at higher O_2 concentration, similar to the case of the first particle in Figure 13*a*. However, as the Y decreases, $\dot{V}_2^*$ increases, a trend which is exactly the opposite from that of the case with a lower O_2 concentration; see Figure 12*b*. As mentioned earlier, the volatiles of low temperature is no longer sufficiently supplied from the first particle when O_2 concentration is increased because the volatiles are mostly consumed. As a result, the combustion due to the volatiles induces the local temperature rise near the second particle, which, in turn, induces a larger $\dot{V}_2^*$. Moreover, enhanced convection effect through the squeezed channel with reducing Y also causes $\dot{V}_2^*$ to increase, whose value reaches nearly $\dot{V}_2^* = 0.95$ for a wide range of X.

3.3. Effects of Inter-Particle Spacing on Total Mass Loss Rate

Figure 14 shows the CO level at two different configurations during char-combustion; the particles in Figure 14*a* are densely situated while the particles in Figure 14*b* are located at a large inter-space distance. When the particles are densely situated, the CO layer, formed by Eqs. (13) and (14), has a tendency to merge together and their merge seems to produce more CO overall. Even for sparsely located particle of Figure 14*b*, the second particle seems to produce more CO than that of the first particle. Here, it is suspected that the CO_2 production of Eq. (6) from the first particle must be adding CO reactant for the endothermic reaction in Eq. (14). This hypothesis is validated in Figure 15, which shows largely distributed CO_2 when enough O_2 supply is allowed with larger X and Y. This CO_2 production from Eq. (6) is combined with char or C and their reaction results in larger CO production at the second particle. Furthermore, since CO production using CO_2 reactant is the endothermic process (see Eq. (14)), the second particle temperature may decrease when CO is overly produced. There will be a cross-point at which this phenomenon of Eq. (14) dominates the effect of oxidation of Eqs. (12) and (13) as in the case of $X = 20$ in Figure 10. Previously, it was shown, in Section 3.2, that increasing X caused the combustion characteristics of the second particle to approach those of the first or single particle; furthermore, the second particle temperature rose. However, when X increased too much, CO_2 production was magnified, and the endothermic reaction of Eq. (14) was also enhanced, which resulted in the reversed pattern in Figure 10.

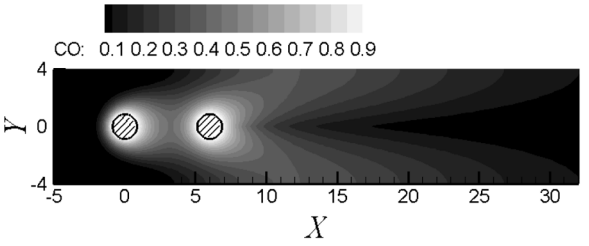

(*a*) X = 6, Y = 8

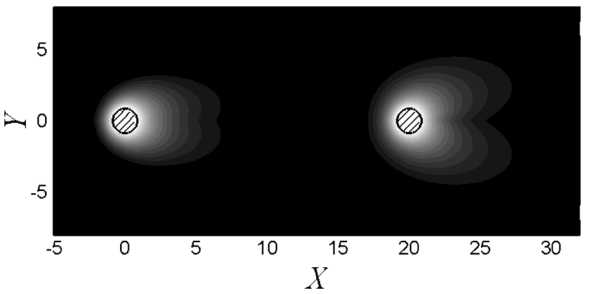

(*b*) X = 20, Y = 20

Figure 14. CO contours for the different particle spacing at 15% O_2 air (25 ms): *a*) $X = 6$, $Y = 8$, *b*) $X = 20$, $Y = 20$.

The effects of X and Y variations on the rate of the particle's total mass loss were investigated. As mentioned, the entire coal particle combustion comprises the devolatilization process (see Eq. (5) of homogeneous reaction) and the subsequent char combustion (see Eqs. (12)–(14) of heterogeneous reaction). The definition of total mass loss includes the mass loss resulting from the devolatilization and char combustion processes. The variable, $dM_{1,2}/dt = \dot{M}_{1,2}$, always less than zero, is used to represent the mass loss rate of the first and second particles, respectively. Here $\dot{M}_{1,2}$ is nondimensionalized by the mass loss rate of a single particle, $\dot{M}_s$, and thus $\dot{M}^*_{1,2} = \dot{M}_{1,2}/\dot{M}_s$. As a result, $\dot{M}^*_{1,2}$ can be greater than unity when the mass loss rate of the first or second particle is greater (due to a certain mechanism, enhanced by X and Y variations) than that of a single particle. We have found that the change in $\dot{M}^*_{1,2}$ becomes more prominent with X and Y variations when O_2 concentration is relatively low (i.e., 15%, rather than any high concentration). Therefore, the results and discussion are largely weighted toward the case with 15% O_2 concentration.

The total mass loss rate of the first particle, $\dot{M}^*_1$, shown in Figure 16*a* indicates that, generally, $\dot{M}^*_1$ is greater than unity for most of the X and Y ranges. When Y is reducing, the convection effect is enhanced and, thus, the total mass loss rate of the first particle increases gradually. However, when Y reaches at around 6, the mass loss rate makes a sudden turn and starts to decrease. The reason for this behavior is that the volatile release rate suddenly increases as $Y < 6$ (see Figure 12*a*) and the reaction of CH_4 with O_2 is expedited. Thus, large amount of CO (see Eq. (6)) is produced. When CO covers the first particle surface (as in Figure 14),

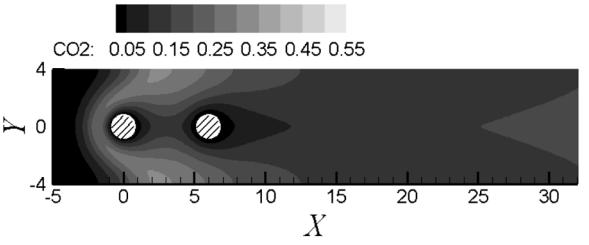

(*a*) X = 6, Y = 8

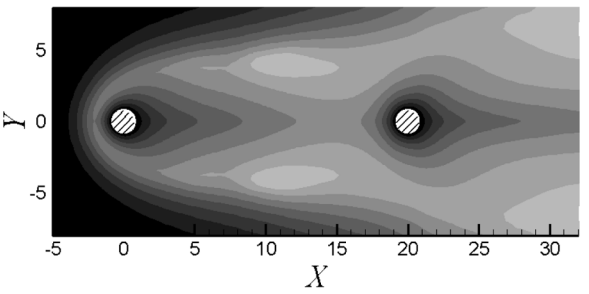

(*b*) X = 20, Y = 20

Figure 15. CO_2 contours for the different particle spacing at 15% O_2 air (25 ms): *a*) $X = 6,\ Y = 8$ and *b*) $X = 20,\ Y = 20$.

O_2 penetration to the particle surface becomes difficult. In this case, efficient char consumption of Eqs. (12) and (13) is prevented. Furthermore, CO itself consumes O_2 during the reaction of Eq. (6). As a result, the mass loss rate is reduced. When Y is relatively large (i.e., $Y \sim 20$) and $X < 8$, $\dot{M}_1^*$ also decreases for the similar reason of the CO layer consuming oxygen, of which phenomenon tends to prevent efficient char combustion.

Figure 16*b* shows the similar trends as the case in Figure 16*a*. The only notable difference is that the mass loss of the second particle is even greater than the single particle mass loss when X and Y are relatively large (i.e., $X > 12$ and $Y > 12$). Although it is expected that the second particle combustion characteristics would converge to the single particle combustion behavior when X and Y are relatively large, large mass loss was observed for the second particle. The reason for this behavior is that the large production of CO_2 from Eq. (6) is combined with char (or C), as in Eq. (14), whose process expedites the mass loss of char (or C).

Figure 17 shows $\dot{M}_1^*$ and $\dot{M}_2^*$ at 50% O_2 concentration. Generally, their change in mass loss is less affected by the X and Y variations because of higher O_2 concentration. Sufficient O_2 supply allows more stable burning and is less susceptible to the geometrical change in the particle location. The decrease in $\dot{M}_1^*$ in Figure 17*a* when $X < 10$ or $Y < 7$ results from the same argument used in Figure 16*a*; the CO layer covering the particle, which causes O_2 depletion and the subsequent burning. When increasing X at smaller Y (i.e., $Y \sim 5$), one noticeable behavior is seen in Figure 17*b*.

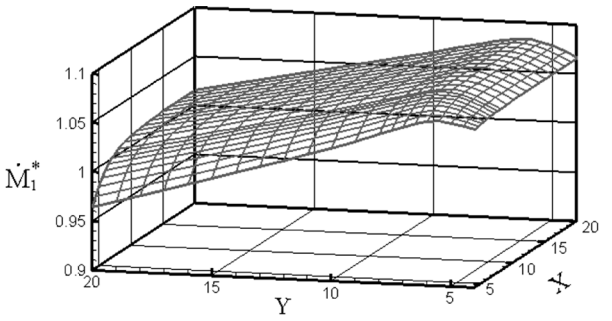

(*a*) 1st particle

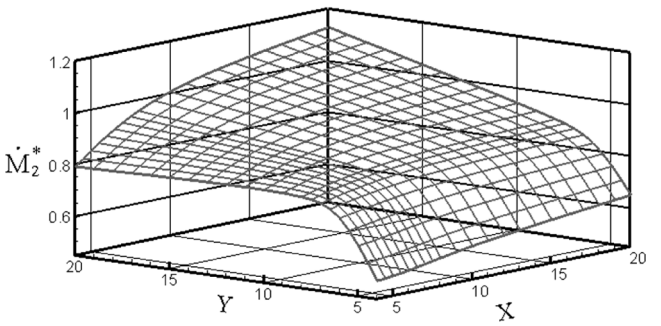

(*b*) 2nd particle

Figure 16. Relative total mass change rate of interacting particle to that of single particle at 15% O_2 air: *a*) first particle and *b*) second particle.

At small Y, flow is accelerated and, thus, O_2 is better supplied. Furthermore, the second particle is less affected by the CO layer released from the first when X is sufficient large. Thus, the mass loss is accelerated as X increases at relatively small Y as shown in Figure 17*b*.

We have correlated the dimensionless volatile release rate ($\dot{V}_1^*$) and the total mass loss rate ($\dot{M}_1^*$) relations shown in Figures 12, 13, 16, and 17. The correlations are as follows.

$$\dot{V}_{1,2}^* = C_1 \chi^{C_2} X^{C_3} Y^{C_4} \tag{25}$$

$$\dot{M}_{1,2}^* = C_1 \chi^{C_2} X^{C_3} Y^{C_4} \tag{26}$$

Here, χ is the mole fraction of O_2. The coefficients, $C_{1,2,3,4}$ presented in Table 4 are applicable for the following range of the parameters, $0.15 \leq \chi \leq 0.95$, $4 \leq X \leq 20$ and $4 \leq Y \leq 20$. The correlations are accurate within 5% error in most X and Y domains. Near boundaries, the accuracy tends to decrease down to around 10%.

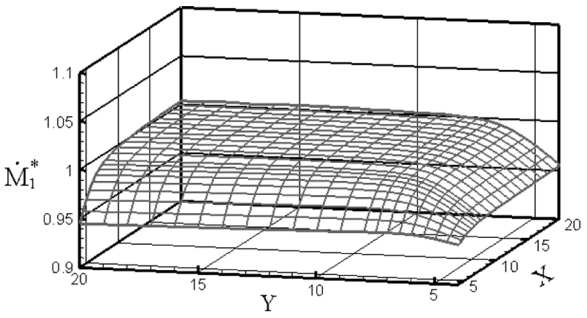

(*a*) 1st particle

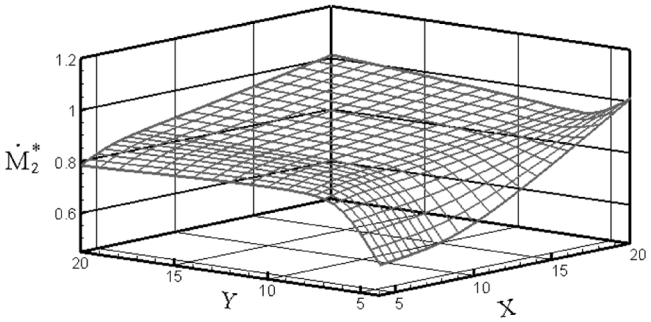

(*b*) 2nd particle

Figure 17. Relative total mass change rate of interacting particle to that of single particle at 50% O_2 air: *a*) first particle and *b*) second particle.

4. CONCLUSIONS

The combustion characteristics of the evenly arranged coal particles at various O_2 concentration levels were numerically investigated to address the influence of the geometrical variance on devolatilization and the char burning rate. The numerical results showed that the rate of devolatilization and char oxidation of interacting coal particles were influenced by the particle spacing (X and Y) and the O_2 concentration level. The summaries are provided as follows.

Table 4. Coefficients of correlations

Base	Particle	C_1	C_2	C_3	C_4
$\dot{V}^*_{1,2}$	First particle	1.02446	0.00219	0.00228	– 0.01294
	Second particle	0.89668	0.02550	0.02080	– 0.00679
$\dot{M}^*_{1,2}$	First particle	0.91106	– 0.06541	0.01775	– 0.00265
	Second particle	0.48108	0.04618	0.14305	0.13740

When X was reduced:

1. O_2 supply to the second particle was not well carried out due to blocking of the first particle and, thus, the second particle temperature was slightly reduced.
2. The volatile release rate ($\dot{V}_1^*$) of the first particle was reduced for both 15% and 50% O_2 cases because of the accumulated volatile near the in-between region for the region in which Y was not an influencing parameter (i.e., at relatively large $Y \sim 20$).
3. The volatile release rate ($\dot{V}_2^*$) of the second particle was also reduced for both 15% and 50% O_2 cases because of the low temperature volatiles released from the first particle for all of the X range.
4. Both $\dot{M}_1^*$ and $\dot{M}_2^*$ were reduced because the CO layer prevented efficient char combustion by blocking and consuming O_2.

When Y was reduced:

1. Convection effect was enhanced, which resulted in the temperature increase for both the first and second particle at 15% O_2 concentration.
2. Due to the temperature increase, $\dot{V}_1^*$ was also increased.
3. Even though the temperature of the second particle increased, $\dot{V}_2^*$ decreased because of the large amount of the volatiles emitted from the first particle.
4. When O_2 concentration was higher (50%), both $\dot{V}_1^*$ and $\dot{V}_2^*$ increased. Little volatiles traveled from the first particle because most were immediately consumed due to the high O_2 level; it did not affect the second particle located downstream.
5. Generally, $\dot{M}_1^*$ increased due to enhanced convection, which provided a large O_2 supply. The char combustion became more efficient. However, $\dot{M}_2^*$ decreased because of the following reasons: first, the earlier consumption of O_2 near the first particle, and, second, the largely accumulated CO layer also prevented the O_2 supply to the second particle.
6. At a higher O_2 concentration, O_2 was better supplied for the second particle with a smaller Y, especially when X was sufficiently large. In this case, the second particle did not experience much O_2 depletion from the first particle. Rather, efficient char combustion occurred with enhanced convection with small Y.

ACKNOWLEDGEMENTS

The authors wish to express their thanks for the financial support made by Combustion Engineering Research Center (CERC) of Korea.

REFERENCES

1. W. P. Hutny, G. K. Lee, and J. T. Price, Fundamentals of Coal Combustion During Injection into a Blast Furnace, *Prog. Energy Combustion Sci.*, vol. 17, pp. 373–395, 1991.
2. L. D. Timothy, D. Froelich, A. F. Sarofim, and J. M. Beer, Characteristics of Single Particle Coal Combustion, *Proc. Combustion Ins.*, vol. 19, pp. 1123–1130, 1982.

3. S. P. Musarra, T. H. Fletcher, S. Nicksa, and H. A. Dwyer, Heat and Mass Transfer in the Vicinity of a Devolatilizing Coal Particle, *Combustion Sci. Tech.*, vol. 45, pp. 289–307, 1986.
4. N. C. Beck and A. N. Hayhurst, The Early Stages of the Combustion of Pulverized Coal at High Temperatures I: The Kinetics of Devolatilization, *Combustion and Flame*, vol. 79, pp. 47–74, 1990.
5. R. He, T. Suda, T. Fujimori, and J. Sato, Effects of Particle Sizes on Transport Phenomena in Single Char Combustion, *Int. J. Heat Mass Transfer*, vol. 46, pp. 3619–3627, 2003.
6. B. E. Poling, J. M. Prausnitz, and J. P. O'Connell, *The Properties of Gases and Liquids*, 5th ed., McGraw Hill, New York, 2001.
7. H. L. Stone, Iterative Solution of Implicit Approximation of Multidimensional Partial Differential Equations, *SIAM J. Numer. Anal.*, vol. 5, pp. 530–558, 1968.
8. C. K. Westbrook and F. L. Dryer, Simplified Reaction Mechanisms for the Oxidation of Hydrocarbon Fuels in Flames, *Combustion Sci. Tech.*, vol. 27, pp. 31–43, 1981.
9. C. P. Cho, Combustion Characteristics of Interacting Fuel Droplets and Coal Particles in Laminar and Turbulent Flow Field, Ph.D. Thesis, Korea University, Seoul, 2007.
10. D. Merick, Mathematical Models of the Thermal Decomposition of Coal: 2. Specific Heats and Heats of Reaction, *Fuel*, vol. 62, pp. 540–546, 1983.
11. H. Kobayashi, J. B. Howard, and A. F. Sarofim, Coal Devolatilization at High Temperatures, *Proc. Combustion Ins.*, vol. 16, pp. 411–425, 1976.
12. Y. C. Guo, C. K. Chan, and K. S. Lau, Numerical Studies of Pulverized Coal Combustion in a Tubular Coal Combustor with Slanted Oxygen Jet, *Fuel*, vol. 82, pp. 893–907, 2003.
13. E. Mon and N. R. Amundson, Diffusion and Reaction in a Stagnant Boundary Layer about a Carbon Particle. 2. An Extension, *Industrial Eng. Chem. Fund.*, vol. 17, pp. 313–321, 1978.
14. I. W. Smith, The Kinetics of Combustion of Pulverized Semi-Anthracite in the Temperature Range 1400–2200 K, *Combustion and Flame*, vol. 17, pp. 421–428, 1971.
15. M. Constanceau and R. Bouard, Experimental Determination of the Main Features of Viscous Flow in the Wake of a Circular Cylinder in Uniform Translation Steady Flow, *J. Fluid Mech.*, vol. 79, pp. 231–256, 1977.
16. J. E. Rengel and S. H. Sphaier, A Projection Method for Unsteady Navier-Stokes Equation with Finite Volume Method and Collocated Grid, *Hybrid Meth. Eng.*, vol. 1(4), pp. 31–56, 1999.
17. J. B. V. Wanderley and C. A. Levi, Validation of a Finite Difference Method for the Simulation of Vortex-Induced Vibrations on a Circular Cylinder, *Ocean Eng.*, vol. 29, pp. 445–460, 2002.